Resolving atomic diffusion in Ru(0001)-O(2 × 2) with spiral high-speed scanning tunneling microscopy

Leonard Gura,[1,*] Zechao Yang,[1,*] Joachim Paier,[2] Florian Kalaß,[1] Matthias Brinker,[1] Heinz Junkes,[1] Markus Heyde,[1,†] and Hans-Joachim Freund[1]

[1]*Fritz-Haber-Institut der Max-Planck-Gesellschaft, Faradayweg 4-6, 14195 Berlin, Germany*

[2]*Humboldt Universität zu Berlin, Unter den Linden 6, 10099 Berlin, Germany*

(Received 20 July 2021; revised 15 October 2021; accepted 14 December 2021; published 11 January 2022)

An intermediate state in atomic diffusion processes in the O(2 × 2) layer on Ru(0001) is resolved with spiral high-speed scanning tunneling microscopy (STM). The diffusion of atomic oxygen in the adlayer has been studied by density functional theory and STM. Transition state theory proposes a migration pathway for the diffusion in the oxygen adlayer. With spiral scan geometries—a new approach to high-speed STM—the oxygen vacancy mobility on the highly covered Ru(0001) surface is determined to be in the range of 0.1 to 1 Hz. Experimental evidence for the intermediate state along the oxygen diffusion pathway is provided in real space and real time.

DOI: 10.1103/PhysRevB.105.035411

I. INTRODUCTION

Surface diffusion governs many elementary processes in nature and technology in connection with surface reactions and catalytic processes as prominent examples [1,2]. One hundred years ago, Volmer and Estermann provided the first experimental evidence for surface diffusion. They observed faster lateral crystal growth from the gas phase than predicted by calculations that neglected mobile species on the crystal surface [3]. Since then a broad variety of methods to study surface diffusion has been developed and applied. During the past decades, observations of atomic hopping events in real space have been reported with scanning tunneling microscopy (STM) [4].

One of the first systems, for which surface diffusion was studied in ultrahigh vacuum (UHV) with chemisorbed species was atomic oxygen on Ru(0001) [1,5]. The system has been studied extensively [6–8] and is a well-suited model system to investigate gas adsorption in general and to apply the knowledge to elucidate mechanisms of catalytic reactions, including water-splitting [9]. In the literature, diffusion rates for chemisorbed oxygen atoms on Ru(0001) are reported for low surface coverages of $\theta = 0.09$ [4]. The coverage θ is defined as the ratio of occupied to accessible hcp sites ($\theta = 1$) on the Ru(0001) surface. For higher coverages, the mobility is expected to decrease due to interaction of the chemisorbed species [4,10]. To the best of our knowledge, so far, the only experimental observation of diffusion processes in an oxygen adlayer on Ru(0001) has been reported by Wintterlin *et al.*, who extracted oxygen vacancy hopping rates in the order of 0.01 to 0.02 Hz from traditional STM measurements with slow scan speeds [10].

For the exposure of molecular oxygen to Ru(0001) in UHV, different superstructures have been reported as a function of temperature and coverage [8,11]. Oxygen dissociates and forms, among other structures, the stable O(2 × 2) structure at room temperature [4,12,13]. The diffusion of oxygen in such ordered adlayers influences the interaction, for example, to water on Ru(0001) [14–17], but also the growth of films, such as silicates [18], silica [19], and graphene [20,21] on this modified substrate. Furthermore, to bridge the pressure gap within basic catalysis research toward catalytic applications, the investigation of highly covered surfaces is a promising approach. In recent studies on the highly covered Ru(0001) surface, the importance of density fluctuations for surface diffusion mechanisms has been revealed. According to the STM measurements, density fluctuations within a CO layer adsorbed on Ru(0001) open low activation energy pathways for the diffusion of coadsorbed atomic oxygen [22]. The experimental results are supported by kinetic Monte Carlo simulations [23].

Another interesting aspect is the surface diffusion at elevated temperatures. A recent study focusses on the dynamics of atomic oxygen on Ru(0001) at 700–950 K with oxygen coverages of $\theta = 0.09$. To study the low-coverage atomic diffusion, the authors used ^{3}He spin echo spectroscopy (^{3}HeSE) and report an activation barrier of 0.385 eV [24]. This barrier is low compared to previous studies [4,25,26]. In addition, Kelsall *et al.* use the noninteracting hcp/fcc jump model [27] and the Bayesian method [28] to extract minority fcc and majority hcp site residence times. The authors conclude that less stable fcc hollow sites are occupied at high temperatures

*These authors contributed equally to this work.
†heyde@fhi-berlin.mpg.de

[24]. The question arises whether or not oxygen atoms occupy less stable sites along their diffusion pathway also at room temperature and whether or not they can be resolved in real space and real time.

In the present study, we examine a diffusion pathway for atomic oxygen within the O(2 × 2) layer on Ru(0001) based on calculations and experiments. Density functional theory (DFT) together with Eyring's transition state theory are used to propose the pathway due to its ability to determine hopping rates accurately [29]. To compare theory to experiment, we performed high-speed STM measurements with an innovative spiral scan geometry and determined the hopping rates of oxygen vacancies in the O(2 × 2) layer on Ru(0001).

The experimentally determined hopping rates are four orders of magnitude higher than theoretical rates considering the highest saddle point along the diffusion pathway. However, within error margins of currently attainable accuracy using orbital-dependent density functionals, the hopping rates deduced from the rate limiting free-energy barrier predicted by theory agree very well with the experimentally observed oxygen vacancy mobility.

The experimental results indicate higher oxygen vacancy mobilities in the O(2 × 2) layer than reported in the literature [10]. Furthermore, we provide the first experimental evidence in real space and real time of the proposed intermediate state on the oxygen diffusion pathway.

II. THEORETICAL MODELING AND EXPERIMENTAL DETAILS

The calculations were carried out using the Vienna *ab initio* simulation package (VASP) [30,31]. Electronic and atomic structure optimizations employ the projector-augmented-wave (PAW) approach to describe the interaction between ionic cores and valence electrons. Spin-nonpolarized Kohn-Sham-Schrödinger equations within DFT employ the strongly constrained and appropriately normed (SCAN) [32] meta-generalized-gradient-approximation to describe electronic exchange and correlation effects. According to the literature [33], SCAN outperforms most of the conventionally used GGA functionals. Especially for activation barriers involving hydrogen transfer, SCAN performs more accurately than GGAs [33]. However, its performance with respect to kinetic parameters involving transfer of heavier atoms like oxygen is not *a priori* guaranteed. Therefore we also employed the adiabatic-connection-fluctuation-dissipation theorem (ACFDT) [34] within the random-phase approximation (RPA) [35,36]. The RPA calculations use PBE orbitals and orbital energies to compute the exact exchange (EXX) and correlation (RPAC) energy contributions [37]. These calculations use the hcp and transition structures optimized by virtue of a O(2 × 2) Ru(0001) surface unit cell.

In the literature, the diffusion process including metastable states is discussed (i) considering the highest saddle point on the energy surface [38] and (ii) evaluating the highest energy barrier height along the diffusion path [39]. Both approaches have been pursued in our calculations. The comparison with the present experiments clearly favors approach (ii), i.e., the highest energy barrier height along the diffusion path determines the jump frequencies. Further technical details of the theoretical calculations can be found in Sections 1, 2, 3, 5, and 6 of the Supplemental Material [40] and in references [41–44] therein.

Within the experimental studies, we used a custom-built high-speed STM with a PtIr tip. The microscope is based on the Pan-STM [45] and benefits from its compact, rigid, and highly symmetric design. We can operate the STM in both conventional and high-speed mode with separate electronic hardware and software [46,47]. In high-speed measurements, the STM operates in quasiconstant height mode. A slow feedback loop corrects for thermal drift, while within one high-speed STM image the height can be assumed as constant. The input signal for the scanner movement is fully customizable. Various spiral scan geometries can be realized, with the most favorable being constant angular velocity (CAV) scans [47]. In the present study we use the Archimedean spiral geometry with constant angular tip velocity. The measurements consist of inward and outward spiral scans. For inward scans, the STM tip starts at the rim and circulates to the center. Once the tip has reached the center, the outward scan starts without interruption. We ensured smooth transitions from inward to outward and from outward to inward scan directions [47].

The experiments were performed in UHV at a base pressure in the range of 10^{-9} mbar. The Ru(0001) single crystal was cleaned by repeating cycles of Ar^+ bombardment, annealing in UHV at 1400 K for 1 min and annealing in oxygen atmosphere (3×10^{-6} mbar) at 1250 K for 20 min. Oxygen was deposited with a 2.5×10^{-6} mbar oxygen atmosphere at 1250 K for 10 min. Subsequently, the sample was cooled in oxygen atmosphere below 360 K within 25 min. Finally, to adjust the oxygen coverage, the sample was flashed in UHV (3×10^{-9} mbar) to 1200 K. This results in the O(2 × 2) coverage on the atomically flat Ru(0001) surface. STM measurements are performed at 300 K.

III. RESULTS AND DISCUSSION

To estimate the atomic hopping frequency, we performed DFT calculations on a 3O(4 × 4) structure, as shown in Figure 1(a). This structure resembles single oxygen vacancies in a closed O(2 × 2) layer. The adsorbed oxygen atoms sit on the threefold hollow (hcp) sites [48]. The oxygen position in the transition structure between O located at this global minimum and O located at the fcc site is the bridge position. For this bridge position, we carried out a vibrational analysis and optimized the transition structure using the improved dimer method implemented in VASP [49,50]. Figure 1(a) shows the resulting possible migration pathway for an oxygen atom (red) to a vacant hcp site on the (2 × 2) superstructure (blue circle). The individual segments of the pathway are color coded and relate to the plotted free-energy profile in Figure 1(b).

The free-energy barriers are calculated with SCAN include zero-point vibrational energy (ZPVE), thermal energy contributions, and vibrational entropy effects at 300 K. The hcp sites on the (2 × 2) lattice resemble global minima. The hcp site on the (1 × 1) lattice and the fcc sites are less stable, resembling local minima on the potential energy surface. The hcp(1 × 1) site exhibits free energies of 0.41 eV as shown in Figure 1(b). The (forward and backward) free-energy barriers between the hcp(1 × 1) site and the transition state at 1.13 eV amount to

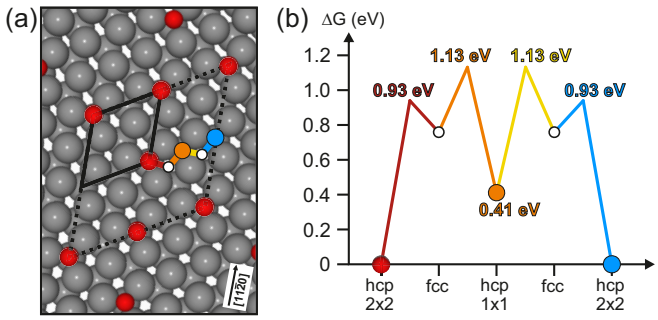

FIG. 1. Possible migration pathway for the oxygen diffusion on Ru(0001) and its corresponding free-energy diagram. (a) A 3O(4×4) structure on Ru(0001) with the unit cell for the DFT calculations marked with a dotted line and the (2×2)-unit cell drawn with a continuous black line. Oxygen atoms are drawn red and the exemplary oxygen vacancy is drawn in blue. The proposed migration pathway is highlighted with colored line segments. (b) Corresponding free-energy diagram corrected for ZPVE, thermal energy contributions for 300 K, and vibrational entropy effects. The color code is adapted from (a).

0.72 eV. The transition state between the hcp(2×2) and the fcc site exhibits the highest free-energy barrier with 0.93 eV. All other steps have substantially lower barriers. Therefore the rate determining free-energy barriers for the diffusion process are 0.93 eV. The barriers are identical by symmetry. Technical break criteria, as, e.g., the maximum atomic force criterion of 0.04 eV/Å employed to determine or localize the transition structure, leads to uncertainties within 0.02 eV. This uncertainty is well below the energy range of interest. Therefore, the energy barriers shown in Figure 1(b) are converged to within significant digits.

To assess rate determining barriers, the RPA approximation is used. The free-energy barrier between the hcp site and the hcp-fcc transition state is 0.14 eV smaller than the respective SCAN-barrier. The RPA corrected rate determining barriers, hence, are 0.79 eV. These values and the energy difference between hcp and fcc sites are in good agreement with reported diffusion barriers of chemisorbed oxygen on Ru(0001) [4,25]. The RPA-corrected overall barrier amounts to 0.99 eV. Despite its systematic underestimation of nonhydrogen transfer barriers in molecular reactions of approximately 0.1 eV, RPA generally improves transfer barrier heights compared with GGA [51].

Following Eyring's transition state theory [52], a rate constant (of first order) k_1^0 is defined that satisfies

$$k_1^0 = \frac{k_B T}{h} e^{\left(-\frac{\Delta G_0^{\neq}}{k_B T}\right)}; \tag{1}$$

k_B is the Boltzmann's constant, h is the Planck's constant, T is the temperature, and $G_0^{\neq}$ is the Gibbs free energy.

The rate constant is the inverse of the average residence time τ.

$$\tau = \frac{1}{k_1^0}. \tag{2}$$

Following approach (i) and considering the overall energy barrier of 0.99 eV at 300 K, jump frequencies of oxygen atoms in the O(2×2) layer in the order of 0.0001 Hz would result. Thus, on average, one jump event in 10,000 s is expected. However, this is by two orders of magnitude slower, in stark contrast to the observations in the literature conducted with slow STM measurement [10]. At room temperature we can assume that the heat transport from the underlying metal substrate is sufficient to populate the hcp(1×1) site by diffusing oxygen [53–56]. Due to the high thermal conductivity of the Ru metal and the resulting very fast heat flux, this process does not compete with the kinetic steps to overcome the energy barriers along the diffusion path and the highest free-energy barrier can be considered as rate determining as outlined in approach (ii). The highest free-energy barrier of 0.79 eV results in rate constants of 0.33 Hz. This corresponds to average residence times τ of approximately 3 s. In contrast to the jump frequencies deduced from the overall barrier, these values are more than 10 times higher than experimentally observed jump frequencies for oxygen vacancies [4,10]. High oxygen vacancy mobilities would be in line with the low activation energy for oxygen diffusion on Ru(0001) deduced from ^{3}HeSE measurements [24].

The question arises whether this high mobility and the fast dynamics are present in the high coverage O(2×2) layer on Ru(0001) and whether or not they can be resolved in real space.

To identify atomic dynamics at the subsecond timescale in real space, the imaging speed of STM must be increased. We achieved this goal by using the high-speed electronics of our custom-built STM and by applying an innovative spiral scan pattern [47].

The conventional raster and the high-speed spiral scan trajectories are schematically shown in Figs. 2(a) and 2(b), respectively. Triangles represent data points and indicate the tip propagation direction. Figure 2(c) shows the conventional scan in constant current mode of the O(2×2) structure. Oxygen atoms appear bright and form a periodic lattice with the unit cell drawn in orange. A defect-free O(2×2) layer would correspond to an oxygen coverage of $\theta = 0.25$. The dark areas in Figure 2 are vacant sites in the regular structure. Including those oxygen vacancies, the oxygen coverage is approximately $\theta = 0.23$. The bright "dashes" in the dark areas indicate atomic movement. Figure 2(d) shows the same surface scanned with the spiral geometry at quasiconstant height. It is the first high-speed STM image acquired with a spiral scan pattern. The acquisition took 50 ms. This is 2000 times faster than for the conventional scan in Figure 2(c). Both spiral and raster scan images show the same atomic arrangement. Due to the improved time resolution of the spiral scan, the vacant sites are free of "dashes" and the hopping of atomic sites can be monitored in real time. Acquisition times and hopping rates are determined based on the installed real time operating system [46,47]. The resulting video of such an image series at a frame rate of 20 Hz is provided in the Supplemental Material [40].

To observe individual hopping events, consecutive high-speed STM images are analyzed as shown in Figs. 3(a) and 3(b). Each image is recorded in 50 ms (that is, a frame rate of 20 Hz). The atomic species are marked with red (oxygen atoms) and blue dots (oxygen vacancies). Comparing the atom positions in Figs. 3(a) and 3(b), two atomic jumps are

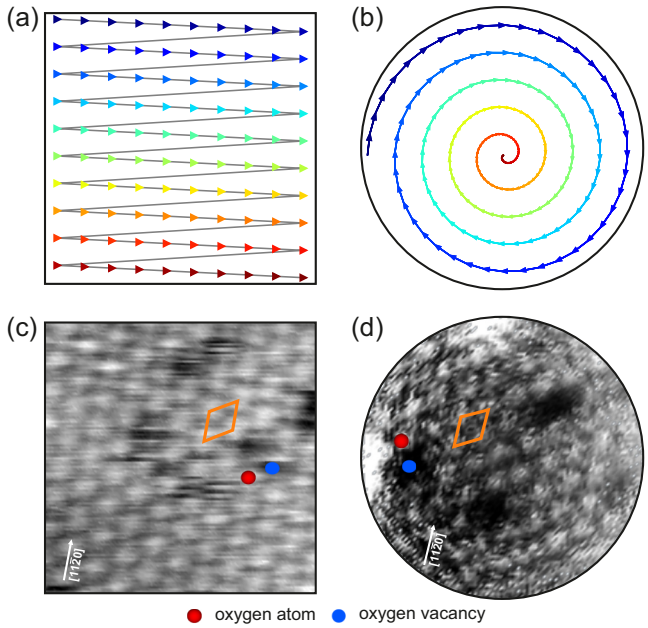

FIG. 2. Raster and spiral scan STM images. (a) Schematic raster scan trajectory. The triangular shaped data points indicate a forward downward scan. (b) Schematic spiral scan trajectory of an Archimedean spiral at CAV. The triangles indicate the inward scan direction. The data point density in the center is increased due to the lower linear velocity of the tip. (c) and (d) Atomically resolved STM images of the O(2 × 2) layer on Ru(0001) ($V_S = 1$ V, $I_T = 1.4$ nA, T = 300 K). (c) Raster scan STM image acquired in constant current mode in 100 s (scan area = 5 nm × 5 nm). (d) High-speed spiral scan STM image acquired in quasiconstant height mode in 50 ms (scan diameter = 5 nm). Oxygen and oxygen vacancy positions are marked exemplarily. The unit cell is drawn in orange.

observed. The atomic species involved are marked with white circles. One jump occurs at the rim of the frame. Here an oxygen atom jumps anticlockwise to the adjacent empty site, while the tip scans clockwise. The second jump occurs closer to the center of the spiral. The observation of two independent jump events within the acquisition time of 50 ms indicates a high mobility in the O(2 × 2) layer. The high mobility is confirmed by additional measurements and observations of jump events over two (2 × 2) lattice sites within 50 ms.

To quantify the experimentally observed dynamics in the O(2 × 2) layer, every individual atomic site is tracked as a function of time. The resulting trajectories are plotted on top of the spiral STM image in Figure 3(c). They show that the jumps occur in all directions—independent of the scan direction of the tip. As obvious from the example of Figs. 3(a) and 3(b), jumps are observed throughout the whole scan area—from the center to the rim. Due to the Archimedean spiral geometry and the CAV mode, the tip spends more time in the center of the scanned area and moves faster at the rim. The varying linear velocity and residence times of the tip as a function of space do not have an influence on the jump rates. These observations confirm that the tip does not significantly affect the thermally activated hopping events.

The vacancies exhibit jump frequencies in the order of 0.1 to 1 Hz, which corresponds to residence times of 10 to 1 s, according to Eq. 2. Figure 3(c) allows to judge on the jump rates and residence times as a function of time and space. An extreme example is found at position *1*, where the vacancy is not visited within the acquisition time of 53.65 s. The low mobility of this particular vacancy is in agreement with the low jump frequency deduced from the theoretical overall barrier of 1.13 eV. Furthermore, this observation is in line with reported jump rates of 0.01–0.02 Hz, which correspond to residence times of 100 and 50 s, respectively [10]. Its adjacent vacancy at position *2*, in contrast, exhibits a jump frequency of 0.60 Hz. The oxygen vacancy mobility in a closed O(2 × 2) layer is expected to be higher than the mobility of the six individual adjacent oxygen atoms. In the example of the vacancy at position *2*, it is obvious from Fig. 3(c) that two oxygen atoms contribute to the hopping events. The hopping rates of these two oxygen atoms are 0.34 and 0.26 Hz, respectively. These values are in very good agreement with the rates deduced from the calculated rate limiting free-energy barriers of 0.33 Hz.

Other vacancies in Fig. 3(c) exhibit jump rates of 0.5–1.6 Hz. The experimentally determined jump rates are more than 10,000 times higher than frequencies deduced from the overall energy barrier following approach (i) described above. On the other hand, the frequencies calculated based on the assumption (ii) that the highest energy barrier is rate determining are in the same range as the experimentally observed jump rates. These jump rates are 10 to 100 times higher than the literature values [4,10].

A broad distribution of the experimentally observed jump rate is expected due to the stochastic nature of the thermally activated processes. In addition to the stochastic aspects, the mobilities of individual oxygen vacancies might be affected by structural features of the topmost Ru(0001) layers. The trajectory in Fig. 3(c) of the vacancy starting at position *3* shows that the jump rate of an individual vacancy can vary over time and as a function of space. This particular vacancy jumps from position *3* to position *4* within 16.7 s, which corresponds to a jump rate of 0.54 Hz. In the subsequent 14 s, the same vacancy rests at position *4*. As mentioned above, this could be related to structural defects in the underlying Ru layers. In addition, the chemical surrounding inside the adsorbed O(2 × 2) layer, i.e., adjacent vacancies, might affect the mobility.

To analyze the effect of adjacent vacancies, the neighborhood of individual vacancies is tracked. Figure 3(d) illustrates the jumps performed by two vacancies (blue and orange lines). The adjacency of the vacancies is plotted over time. Within the acquired time, they appear as either single vacancies (0 adjacent vacancies) or exhibit one (1) adjacent vacancy. The horizontal lines represent residence times in a certain configuration (0 or 1 adjacent vacancy). The vertical lines represent changes in the configuration, i.e., from 0 to 1 adjacent vacancy or vice versa. The residence time in each configuration is similar, and jumps toward another vacancy happen as frequent as jumps away from an adjacent vacancy. For a preferred configuration, larger residence times would be expected. Accumulating the residence times, the two vacancies spend 45 to 65% of the time in the configuration with one adjacent vacancy. The theoretical probability p_{VV} that two oxygen vacancies are adjacent is given in Eq. (3); c_V is

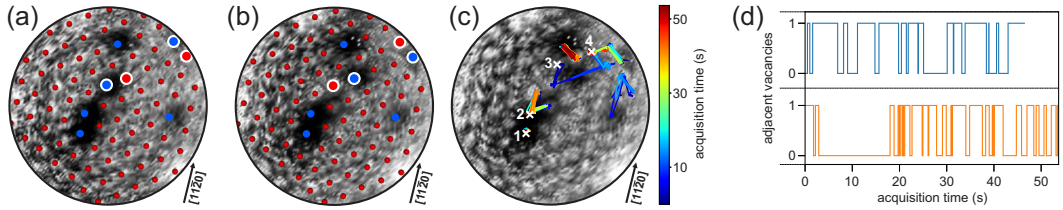

FIG. 3. Sequence of atomically resolved STM images of the O(2 × 2) layer on Ru(0001) ($V_S = 1$ V, $I_T = 1.4$ nA, T = 300 K, scan diameter = 5 nm). (a) Frame at $t = 0$ ms. (b) Frame at $t = 50$ ms. (c) Oxygen vacancy trajectories over the acquisition time of 53.65 s. (d) Evolution of the adjacency of two independent oxygen vacancies (blue and orange lines). At the configuration *0 adjacent vacancies*, the vacancy is surrounded by six oxygen atoms. At the configuration *1 adjacent vacancies*, the vacancy is surrounded by five oxygen atoms and one oxygen vacancy.

the oxygen vacancy concentration. The factor of 6 represents the number of nearest neighbors in the hexagonal O(2 × 2) structure.

$$p_{VV} = 6c_V \tag{3}$$

At oxygen coverages of $\theta = 0.23$, the vacancy concentration c_V is 0.08. With this vacancy concentration, the theoretical probability p_{VV} that two vacancies are adjacent is 48%. This value is within the experimentally determined range. This agreement and the observation of frequently changing vacancy adjacencies indicate that no configuration is preferred compared to the other. A more detailed study of the oxygen vacancy mobility in dependence on the nearest neighborhood is an interesting study for future experiments.

While for the diffusion within the chemisorbed systems solely the occupation of adsorption sites and a rigid hopping between these discrete sites is expected [1], the suggested migration pathway in Fig. 1 includes the threefold hollow hcp and fcc sites as intermediate states. In principle, these intermediate states should be occupied for a certain albeit very short time. Kelsall *et al.* detected the occupation of the fcc site at high temperatures with ^{3}HeSE [24]. The question arises whether or not the intermediate state along the migration pathway can also be resolved in real space.

The applied spiral geometry for the high-speed scan has two important advantages in terms of spatial and time resolution in the center of the frame: First, the data point density in the center of the Archimedean spiral is increased at CAV, as schematically shown in Fig. 2(b). Second, the continuous scan direction for consecutive frames enables a smooth transition from the inward to the outward scan direction.

Three consecutive spiral STM images, each acquired in 50 ms, reveal dynamics in the central region. The region of interest is marked in Figs. 4(a)–4(c) with white circles. This section of the full spiral scan was acquired in 16 ms. For visualization, Figures 4(d)–4(f) show the magnified STM images at time $t_d = 0$ ms, $t_e = 16$ ms, and $t_f = 84$ ms, respectively. Figure 4(d) is extracted from the inward scan in Fig. 4(a). The consecutive image in Fig. 4(e) shows the outward scan and is acquired in the subsequent 16 ms.

Within the time interval of 16 ms, a local change in the image contrast between Figs. 4(d) and 4(e) is observed, indicating a hopping event. This observation is possible because of a special advantage of the spiral scan technique over conventional linear scan methods: When the spiral scan direction in the spiral center is reversed in going from inward to outward spiral scan, the elapsed time between the observation of a diffusion event close to the center of the spiral is much shorter than the time to scan the whole image area. Consequently, jump events within time intervals shorter than 16 ms become observable. For visualization, the structural models

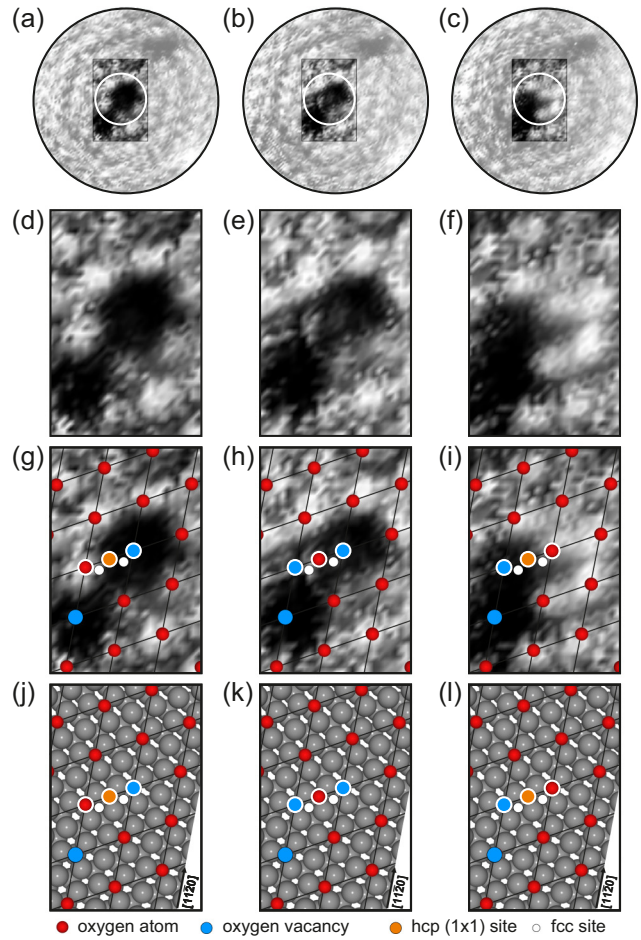

FIG. 4. Resolved intermediate state. (a)–(c) Three consecutive spiral STM images (i.e., in-, out-, inward scan), each acquired in 50 ms ($V_S = 1$ V, $I_T = 1.4$ nA, T = 300 K, scan diameter = 5 nm, highlighted scan area = 2.2 nm × 1.4 nm). The region of interest in the white circle is acquired in 16 ms. The highlighted scan areas from (a) to (c) are magnified in (d)–(f), respectively. (g)–(i) STM images overlaid with corresponding structural models. (j)–(l) Corresponding structural models including the substrate.

in Figs. 4(g) and 4(h) illustrate the process and directly relate to the proposed migration pathway in Fig. 1. The involved atomic sites are marked with white circles. In Fig. 4(e), both (2×2) hcp sites show decreased intensities and appear to be vacant (blue circles with white outlines). At the same time, the intensity at the intermediate position between the two vacant sites increases (here we look at the oxygen atom migrating to the vacant hcp site which is equivalent to a mobile oxygen vacancy moving in the reverse direction).

A possible explanation for the observed phenomenon Fig. 4 would be that the STM tip captures the first part of the oxygen atom. Then the atom jumps to the vacant site that was already scanned. Following this scenario, imaged oxygen atoms of different sizes would be expected depending on the time when the oxygen atom jumped away under the tip. However, the fact that comparable image contrasts were observed several times at the same spatial positions with respect to the surrounding oxygen atoms implies that the observed image contrast is not caused by jumps at random times.

The characteristic lateral position of the experimentally observed intermediate state during the jump event coincides very well with the hcp site on the (1×1) grid that is part of the suggested diffusion pathway based on DFT calculations. Subsequently, the oxygen atom jumps to the adjacent vacant (2×2) hcp site in Fig. 4(f). These observations provide clear evidence for the occupation of the intermediate state on the (1×1) hcp site.

IV. CONCLUSION

To summarize, a combination of DFT-based calculations and high-speed STM have demonstrated increased oxygen vacancy mobilities in the chemisorbed $O(2 \times 2)$ layer on Ru(0001). The spiral scan geometry application in the present high-speed STM allowed us to observe, for the first time, the intermediate state along the diffusion pathway of oxygen in the $O(2 \times 2)$ layer in real time and real space. This achievement extends considerably the existing STM techniques and shows the potential to decipher diffusion and migration processes at the atomic scale and at submillisecond timescales.

ACKNOWLEDGMENTS

The authors thank Joost Wintterlin and Wolf-Dieter Schneider for fruitful discussions. This project has received funding from the European Research Council (ERC) under the European Unions Horizon 2020 Research and Innovation Program (Grant Agreement No. 669179). Leonard Gura acknowledges support by the IMPRS for Elementary Processes in Physical Chemistry. Joachim Paier gratefully acknowledges Professor Joachim Sauer for permission to use some of his computational facilities. Furthermore, support by the North-German Supercomputing Alliance (HLRN) is gratefully acknowledged for providing HPC resources that have contributed to the research results reported in this paper.

[1] A. Kapoor, R. T. Yang, and C. Wong, Surface diffusion, Catalysis Rev. Sci. Eng. **31**, 129 (1989).

[2] A. G. Naumovets, Collective surface diffusion: An experimentalist's view, Phys. A Stat. Mech. Appl. **357**, 189 (2005).

[3] M. Volmer and I. Estermann, Über den Mechanismus der Molekülabscheidung an Kristallen, Z. Phys. **7**, 13 (1921).

[4] J. Wintterlin, J. Trost, S. Renisch, R. Schuster, T. Zambelli, and G. Ertl, Real-time STM observations of atomic equilibrium fluctuations in an adsorbate system: O/Ru(0001), Surf. Sci. **394**, 159 (1997).

[5] J. A. Schreifels, S.-K. Shi, and J. M. White, The effect of electron beam and surface diffusion on the kinetics of adsorbed oxygen reacting with hydrogen on Ru(001), Appl. Surf. Sci. **7**, 312 (1981).

[6] M. C. Wheeler, D. C. Seets, and C. B. Mullins, Kinetics and dynamics of the initial dissociative chemisorption of oxygen on Ru(001), J. Chem. Phys. **105**, 1572 (1996).

[7] P. Piercy, K. De'Bell, and H. Pfnür, Phase diagram and critical behavior of the adsorption system O/Ru(001): Comparison with lattice-gas models, Phys. Rev. B **45**, 1869 (1992).

[8] H. Over, Surface chemistry of ruthenium dioxide in heterogeneous catalysis and electrocatalysis: From fundamental to applied research, Chem. Rev. **112**, 3356 (2012).

[9] F. M. Sapountzi, J. M. Gracia, C. J. K.-J. Weststrate, H. O. A. Fredriksson, and J. W. H. Niemantsverdriet, Electrocatalysts for the generation of hydrogen, oxygen and synthesis gas, Prog. Energy Combust. Sci. **58**, 1 (2017).

[10] H.-J. Güntherodt and R. Wiesendanger, *Scanning Tunneling Microscopy I: General Principles and Applications to Clean and Adsorbate-Covered Surfaces* (Springer, Berlin, Heidelberg, 1992).

[11] N. Nilius, M. Mitte, and H. Neddermeyer, Low-temperature scanning tunnelling microscopy study of O_2 adsorption on Ru(0001), Appl. Phys. A **66**, S519 (1998).

[12] T. E. Madey, H. Albert Engelhardt, and D. Menzel, Adsorption of oxygen and oxidation of CO on the ruthenium (001) surface, Surf. Sci. **48**, 304 (1975).

[13] M. Lindroos, H. Pfnür, G. Held, and D. Menzel, Adsorbate induced reconstruction by strong chemisorption: Ru(001) $p(2 \times 2) - O$, Surf. Sci. **222**, 451 (1989).

[14] T. K. Shimizu, A. Mugarza, J. I. Cerdá, M. Heyde, Y. Qi, U. D. Schwarz, D. F. Ogletree, and M. Salmeron, Surface species formed by the adsorption and dissociation of water molecules on a Ru(0001) surface containing a small coverage of carbon atoms studied by scanning tunneling microscopy, J. Phys. Chem. C **112**, 7445 (2008).

[15] S. Maier, P. Cabrera-Sanfelix, I. Stass, D. Sánchez-Portal, A. Arnau, and M. Salmeron, Water-induced surface reconstruction of oxygen (2×1) covered Ru(0001), Phys. Rev. B **82**, 075421 (2010).

[16] S. Maier, I. Stass, J. I. Cerdá, and M. Salmeron, Unveiling the Mechanism of Water Partial Dissociation on Ru(0001), Phys. Rev. Lett. **112**, 126101 (2014).

[17] R. Souda and T. Aizawa, Nucleation and growth of water ice on Ru(0001): Influences of oxygen and carbon-monoxide adspecies, Chem. Phys. Lett. **722**, 132 (2019).

[18] E. Emmez, J. Anibal Boscoboinik, S. Tenney, P. Sutter, S. Shaikhutdinov, and H.-J. Freund, Oxidation of the Ru(0001) surface covered by weakly bound, ultrathin silicate films, Surf. Sci. **646**, 19 (2016).

[19] R. Włodarczyk, M. Sierka, J. Sauer, D. Löffler, J. J. Uhlrich, X. Yu, B. Yang, I. M. N. Groot, S. Shaikhutdinov, and

H.-J. Freund, Tuning the electronic structure of ultrathin crystalline silica films on Ru(0001), Phys. Rev. B **85**, 085403 (2012).

[20] T. Li and J. A. Yarmoff, Intercalation and desorption of oxygen between graphene and Ru(0001) studied with helium ion scattering, Phys. Rev. B **96**, 155441 (2017).

[21] E. Voloshina, N. Berdunov, and Y. Dedkov, Restoring a nearly free-standing character of graphene on Ru(0001) by oxygen intercalation, Sci. Rep. **6**, 20285 (2016).

[22] A.-K. Henß, S. Sakong, P. K. Messer, J. Wiechers, R. Schuster, D. C. Lamb, A. Groß, and J. Wintterlin, Density fluctuations as door-opener for diffusion on crowded surfaces, Science **363**, 715 (2019).

[23] S. Sakong, A.-K. Henß, J. Wintterlin, and A. Groß, Diffusion on a crowded surface: KMC simulations, J. Phys. Chem. C **124**, 15216 (2020).

[24] J. Kelsall, P. S. M. Townsend, J. Ellis, A. P. Jardine, and N. Avidor, Ultrafast Diffusion at the Onset of Growth: O/Ru(0001), Phys. Rev. Lett. **126**, 155901 (2021).

[25] A. B. Anderson and M. K. Awad, Binding of Ru, O, and RuOn (n=1-4) to the Ru(001) surface: Structures, stabilities, and diffusion barriers, Surf. Sci. **183**, 289 (1987).

[26] S. Renisch, R. Schuster, J. Wintterlin, and G. Ertl, Dynamics of Adatom Motion Under the Influence of Mutual Interactions: O/Ru(0001), Phys. Rev. Lett. **82**, 3839 (1999).

[27] F. E. Tuddenham, H. Hedgeland, A. P. Jardine, B. A. J. Lechner, B. J. Hinch, and W. Allison, Lineshapes in quasi-elastic scattering from species hopping between non-equivalent surface sites, Surf. Sci. **604**, 1459 (2010).

[28] B. A. J. Lechner, P. R. Kole, H. Hedgeland, A. P. Jardine, W. Allison, B. J. Hinch, and J. Ellis, Ultra-high precision determination of site energy differences using a bayesian method, PRB **89**, 121405(R) (2014).

[29] D.-J. Liu and J. W. Evans, Lattice-gas modeling of the formation and ordering of oxygen adlayers on Pd(100), Surf. Sci. **563**, 13 (2004).

[30] G. Kresse and J. Furthmüller, Efficiency of *ab-initio* total energy calculations for metals and semiconductors using a plane-wave basis set, Comput. Mater. Sci. **6**, 15 (1996).

[31] G. Kresse and J. Furthmüller, Efficient iterative schemes for ab initio total-energy calculations using a plane-wave basis set, Phys. Rev. B **54**, 11169 (1996).

[32] J. Sun, A. Ruzsinszky, and J. P. Perdew, Strongly Constrained and Appropriately Normed Semilocal Density Functional, Phys. Rev. Lett. **115**, 036402 (2015).

[33] J. Sun, R. C. Remsing, Z. Sun, A. Ruzsinszky, H. Peng, Z. Yang, A. Paul, U. Waghmare, X. Wu, M. L. Klein, and J. P. Perdew, Accurate first-principles structures and energies of diversely bonded systems from an efficient density functional, Nat. Chem. **8**, 831 (2016).

[34] D. Langreth and J. Perdew, The exchange-correlation energy of a metallic surface, Solid State Commun. **17**, 1425 (1975).

[35] D. Bohm and D. Pines, A collective description of electron interactions: III. Coulomb interactions in a degenerate electron gas, Phys. Rev. **92**, 609 (1953).

[36] M. Gell-Mann and K. A. Brueckner, Correlation energy of an electron gas at high density, Phys. Rev. **106**, 364 (1957).

[37] J. Harl and G. Kresse, Cohesive energy curves for noble gas solids calculated by adiabatic connection fluctuation-dissipation theory, Phys. Rev. B **77**, 045136 (2008).

[38] I. Matrane, M. Mazroui, and Y. Boughaleb, Diffusion and adsorption of Au and Pt adatoms on ideal and missing row reconstructed surfaces of Au(110): DFT and EAM calculations, Surf. Sci. **677**, 83 (2018).

[39] H. T. Lorensen, J. K. Nørskov, and K. W. Jacobsen, Mechanisms of self-diffusion on Pt(110), Phys. Rev. B **60**, R5149(R) (1999).

[40] See Supplemental Material at http://link.aps.org/supplemental/10.1103/PhysRevB.105.035411 for technical and theoretical details, additional jump analysis, and a real time high-speed spiral STM video.

[41] H. J. Monkhorst and J. D. Pack, Special points for brillouin-zone integrations, Phys. Rev. B **13**, 5188 (1976).

[42] M. Kaltak, J. Klimeš, and G. Kresse, Low scaling algorithms for the random phase approximation: Imaginary time and laplace transformations, J. Chem. Theory Comput. **10**, 2498 (2014).

[43] M. Shishkin and G. Kresse, Implementation and performance of the frequency-dependent *GW* method within the PAW framework, Phys. Rev. B **74**, 035101 (2006).

[44] J. Harl, L. Schimka, and G. Kresse, Assessing the quality of the random phase approximation for lattice constants and atomization energies of solids, Phys. Rev. B **81**, 115126 (2010).

[45] S. H. Pan, E. W. Hudson, and J. C. Davis, ^{3}He refrigerator based very low temperature scanning tunneling microscope, Rev. Sci. Instrum. **70**, 1459 (1999).

[46] H. Junkes, H.-J. Freund, L. Gura, M. Heyde, P. Marschalik, and Z. Yang, Experiment control with EPICS7 and symmetric multiprocessing on RTEMS, in *16th International Conference on Accelerator and Large Experimental Control Systems (ICALEPCS2017)* (JACoW, 2018), pp. 1762–1766.

[47] L. Gura, Z. Yang, M. Brinker, F. Kalaß, W. Kirstaedter, P. Marschalik, H. Junkes, M. Heyde, and H.-J. Freund, Spiral high-speed scanning tunneling microscopy: Tracking atomic diffusion on the millisecond timescale, Appl. Phys. Lett. **119**, 251601 (2021).

[48] H. Over, Crystallographic study of interaction between adspecies on metal surfaces, Prog. Surf. Sci. **58**, 249 (1998).

[49] G. Henkelman and H. Jónsson, A dimer method for finding saddle points on high dimensional potential surfaces using only first derivatives, J. Chem. Phys. **111**, 7010 (1999).

[50] A. Heyden, A. T. Bell, and F. J. Keil, Efficient methods for finding transition states in chemical reactions: Comparison of improved dimer method and partitioned rational function optimization method, J. Chem. Phys. **123**, 224101 (2005).

[51] J. Paier, X. Ren, P. Rinke, G. E. Scuseria, A. Grüneis, G. Kresse, and M. Scheffler, Assessment of correlation energies based on the random-phase approximation, New J. Phys. **14**, 043002 (2012).

[52] M. Henzler and W. Göpel, *Oberflächenphysik des Festkörpers*, 2nd ed. (BG Teubner Verlag, Stuttgart, 1994).

[53] J. Barth, Transport of adsorbates at metal surfaces: from thermal migration to hot precursors, Surf. Sci. Rep. **40**, 75 (2000).

[54] C. Bartels, R. Cooper, D. J. Auerbach, and A. M. Wodtke, Energy transfer at metal surfaces: the need to go beyond the electronic friction picture, Chem. Sci. **2**, 1647 (2011).

[55] S. P. Rittmeyer, V. J. Bukas, and K. Reuter, Energy dissipation at metal surfaces, Adv. Phys.: X **3**, 1381574 (2018).

[56] T. Kropp, J. Paier, and J. Sauer, Support effect in oxide catalysis: Methanol oxidation on vanadia/ceria, J. Am. Chem. Soc. **136**, 14616 (2014).